nature communications

Article

https://doi.org/10.1038/s41467-026-74349-6

# Iodine-mediated proton-coupled electron transfer enables selective polymerization of organic pollutants in an oxidant-free electrocatalytic system

Received: 8 January 2026

Accepted: 3 June 2026

Published online: 15 June 2026

Check for updates

Zexiao Zheng[1], Jin Zhang[1] ✉, Jonathan J. Calvillo Solís[1], Howard Y. M. Cheung[1], Ashutosh Kumar[2], Xiaohong Guan[3], Haoran Dong[4] & Irene M. C. Lo[1,5] ✉

Organic polymerization offers a sustainable water treatment approach that enables resource recovery, yet current oxidant-involved practices suffer from poor selectivity. We present an oxidant-free electrocatalytic system for phenolic pollutant polymerization via iodine-mediated proton-coupled electron transfer (PCET) with an iodine-enriched bismuth-oxyiodide-coated carbon cloth (I-BiOI@CC) anode, achieving 97.1% polymerization selectivity by converting pollutants into insoluble polymerized products. Mechanistic investigations demonstrate that I-BiOI@CC provides reversible redox mediation ($3I^- \leftrightarrows I_3^-$), enhancing pollutant-electrode interaction and accelerating interfacial charge transfer to facilitate PCET-oxidation of phenols to phenolic radicals that undergo polymerization through thermodynamically favored *ortho* C–O coupling. Polymerization kinetics depend on proton and electron transfer energetics, wherein phenols with stronger electron-donating capacity and weaker O–H bond strength promote the PCET process. The electrocatalytic system exhibits high energy and cost efficiency, demonstrates negligible biotoxicity, and shows excellent practicality. This work offers a promising proof-of-concept for future development of green and selective electrocatalytic processes for water decontamination.

Advanced oxidation processes (AOPs) are extensively employed for the degradation of organic pollutants through generating reactive species (e.g., $^{\bullet}OH$ and $SO_4^{\bullet-}$), which oxidatively decompose organic compounds to produce lower-molecular-weight intermediates and, ultimately, carbon dioxide[1–4]. Mechanistically, the complete degradation of organic pollutants necessitates extensive electron transfer (e.g., 100% mineralization of phenol consumes 28 equivalents of electrons)[5–7]. Consequently, AOPs typically demand high oxidant dosages (2–3 orders of magnitude of pollutant concentrations), yet achieve limited total organic carbon (TOC) removal (20–50%), and frequently produce toxic intermediate by-products[8]. Unlike traditional AOPs, polymerization processes convert soluble phenolic pollutants into insoluble and hydrophobic polymerized products via organic radical coupling reactions, offering a sustainable pathway for simultaneous pollutant removal and resource recovery[5,7,9]. From a thermodynamic perspective, polymerization processes proceed with one unit of electron transfer per organic molecule. Consequently, they only require low oxidant dosages (2–10 times that of pollutant concentrations)[10,11], while

[1]Department of Civil and Environmental Engineering, The Hong Kong University of Science and Technology, Hong Kong, China. [2]Department of Energy and Environment, Thapar Institute of Engineering and Technology, Patiala, Punjab, India. [3]School of Ecological and Environmental Sciences, East China Normal University, Shanghai, China. [4]College of Environmental Science and Engineering, Hunan University, Changsha, Hunan, China. [5]Institute for Advanced Study, The Hong Kong University of Science and Technology, Hong Kong, China. ✉e-mail: kim.zhang@connect.ust.hk; cemclo@ust.hk

attaining high TOC removal (>95%) and ecotoxicity reduction (>90%) by converting pollutants into value-added products with mitigated formation of intermediate byproducts[12,13].

Despite the above-mentioned advantages, existing polymerization processes based on powdered catalysts face multiple challenges. First, a kinetic imbalance often arises between oxidant activation and pollutant oxidation, as powdered catalysts must function simultaneously as oxidant activators and pollutant adsorbents. As such, some catalysts rapidly activate oxidants but adsorb phenolic pollutants slowly, whereas others exhibit strong adsorption yet poor oxidant activation[14]. This mismatch leads to oxidant waste and restricted efficiency. Second, they are mired in poor selectivity due to the reliance on oxidative species (e.g., $^{\bullet}OH$ and $SO_4^{\bullet-}$) or high-valence metal-oxo (HVMO) to generate phenoxyl radicals. These uncontrolled reactions can over-oxidize the aromatic structure to reduce polymer yield, and complex wastewater matrices also quench these reactive species to impede the polymerization process[5,11]. Therefore, a paradigm shift in polymerization is required to address the kinetic imbalance and enhance selectivity, thereby unlocking their complete potential.

Electrocatalysis, which anchors electrocatalysts on conductive substrates as electrodes, offers a promising route for water treatment due to its exceptional capacity for precise reaction control[15,16]. Conventional electrolytic systems rely on the anodic oxidation, using anodes like boron-doped diamond or $PbO_2$, to generate reactive oxygen species for pollutant removal through an energy-intensive non-selective mineralization pathway[16]. In contrast, electrocatalytic-driven proton-coupled electron transfer (PCET) that simultaneously transfers an electron and a proton provides an alternative for organic polymerization[17,18]. Upon a moderate potential, organic molecules are oxidized to organic radicals that subsequently undergo polymerization[19]. While electrocatalytic-driven PCET has been extensively developed for chemical synthesis, its potential in water treatment remains to be explored. Notably, PCET-driven polymerization in the electrocatalytic system enables direct pollutant oxidation without external oxidants, where electrocatalysts only serve as pollutant adsorbents. The decoupling of pollutant adsorption and oxidant activation resolves the kinetic imbalance of polymerization using powdered catalysts. As such, the precise design of the anode with a strong affinity towards phenolic pollutants will enable enhanced kinetics and improved polymerization selectivity.

An ideal anode for electrocatalytic polymerization should feature: (i) strong affinity towards phenolic hydroxyl groups for enhanced selectivity; (ii) high charge transfer capacity to sustain anodic oxidation; and (iii) a large surface area to facilitate polymerization reactions[16]. BiOI is a preferable candidate due to its distinctive surface chemistry and catalytic reactivity. Its iodine (I)-terminated surface facilitates the interaction with phenolic hydroxyl groups via a hydrogen bond to iodine ($H^{\delta+}\cdots I^{\delta-}$), enabling selective uptake of pollutants from non-polar wastewater matrices for subsequent reactions[20,21]. Moreover, iodine species ($I^-/I_3^-$) on BiOI act as reversible redox mediators ($3I^- \leftrightarrows I_3^-$), promoting proton and electron transfer to facilitate PCET-driven polymerization[22,23]. However, pristine BiOI suffers from poor charge transfer ability and limited iodine content[24], hindering pollutant uptake and subsequent PCET reactions. I-rich modification is anticipated to overcome these limitations by incorporating excess iodine species within the layered BiOI to strengthen internal electric fields for enhanced charge transfer, increasing iodine active sites to accelerate pollutant adsorption kinetics, and abundant reversible redox mediators for the PCET process[21,25]. Moreover, carbon cloth (CC), with its large surface area, excellent conductivity, lightweight, flexibility, and corrosion-resistance, serves as a suitable conductive substrate[3,26]. Therefore, the I-rich modified BiOI coated CC (I-BiOI@CC) is expected to maximize the efficiency and selectivity of the electrocatalytic polymerization.

Herein, we establish an oxidant-free electrocatalytic system based on an I-BiOI@CC anode, where I-terminated surface initiates PCET to generate phenoxyl radicals for efficient and selective polymerization of phenolic pollutants. The I-BiOI@CC anode integrates selective pollutant uptake, rapid charge transfer, and reversible iodine redox mediation, attaining simultaneous pollutant removal and resource recovery. Comprehensive electrochemical, spectroscopic, and theoretical analyses elucidate the iodine-mediated PCET mechanism, pollutant polymerization routes, and structure-reactivity correlations at the molecular level. Furthermore, sustainability and practicality assessment, in terms of energy- and cost-effectiveness, carbon emissions, biotoxicity, and continuous-flow operation, are also performed to demonstrate application potential.

## Results

### Material characterization and performance assessment

The morphology and chemical structure of the synthesized anodes were characterized using multiple techniques. Scanning electron microscopy (SEM) reveals (Fig. S1) the uniform coating of BiOI and I-BiOI on CC fibers. Pristine BiOI (Fig. 1a) exhibits a nanosheet-packed flower-like structure with a large surface area for electrocatalytic reactions. In contrast, I-BiOI maintains a similar architecture but shows nanoparticle-coated nanosheets with rough surfaces, resulting from the deposition of excessive iodine species on the BiOI surface. High-resolution transmission electron microscope (HRTEM) analysis illustrates the well-crystallized I-BiOI with lattice fringes of 0.28 nm, corresponding to the (110) plane (Fig. 1b, raw FFT image is provided in Fig. S2e)[27]. Notably, a distinct I layer surrounds the lattice fringes of BiOI, confirming successful I enrichment with increased exposure of iodine species. Elemental mapping (Fig. S2a–d) verifies the uniform distribution of Bi, O, and I in I-BiOI. Moreover, I-BiOI exhibits a reduced surface wettability with a contact angle of ~77° (Fig. S3) compared to BiOI (~71°) due to the excessive I loading altering material surface wax chemistry. X-ray diffraction (XRD) spectra (Fig. S4) show well-crystallized BiOI and I-BiOI, with the (110) facet dominating, which matches the TEM observation. I-BiOI exhibits lower facet intensity than BiOI, attributed to the mitigated signal reflection raised from the I layer. The XPS survey spectra display the same elemental composition for BiOI and I-BiOI (Fig. S5). The high-resolution I 3 d XPS spectra (Fig. 1c) show that I-BiOI attains an increased I loading amount, ~1.38-fold that of BiOI. A 0.5 eV positive shift of binding energy is observed for I-BiOI, demonstrating that I enrichment alters material electronic structure and enhances Bi-I bonding interactions[20]. This finding is further evidenced by Fourier transform infrared (FTIR) analysis (Fig. 1d) and Raman spectra (Fig. S6), where I-BiOI exhibits a significantly stronger intensity for Bi-I stretching vibrations than BiOI. Collectively, during I enrichment modification, a portion of iodine is incorporated into the BiOI lattice, and the remainder is distributed over the BiOI surface, thereby altering the chemical and electronic configuration of BiOI.

The electrochemical analysis was performed to study how I enrichment alters the charge transfer ability and surface reactivity of the material. Electrochemical impedance spectroscopy (EIS, Fig. 1e) with the presence of acetaminophen (ACE, a representative of phenols) illustrates that the fitted charge-transfer resistances (*Rct*) are 10.0 and 4.0 Ω for BiOI@CC and I-BiOI@CC, suggesting I enrichment significantly enhances the materials' charge transfer ability. This improvement is attributed to the incorporation of excess iodine species within the layered BiOI, which strengthens the electric field intensity and facilitates more efficient charge transfer[21,28]. Additionally, the shortened Warburg tail (45° back slope) observed for the EIS spectrum of I-BiOI@CC indicates that the I enrichment enhances ionic diffusion, enabling more effective interaction between ACE molecules and I-BiOI@CC for subsequent polymerization. Derived from the cyclic voltammetry (CV) curves at different scan rates (Fig. S7), the double-layer capacitance ($C_{dl}$) of I-BiOI@CC anode is determined as 1.94 mF $cm^{-2}$ (Fig. 1f), ~1.36-fold that of BiOI (1.42 mF $cm^{-2}$), providing

https://doi.org/10.1038/s41467-026-74349-6

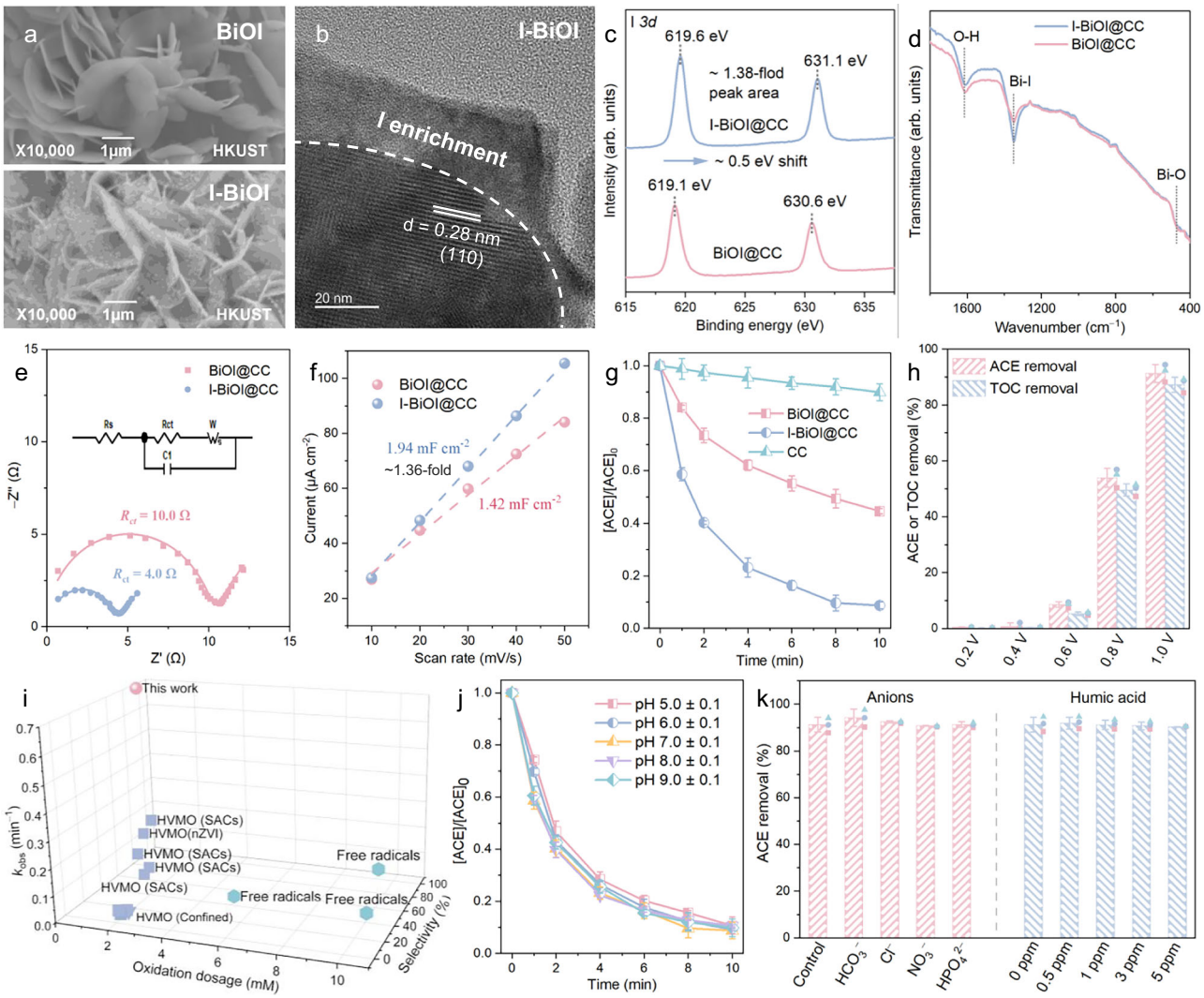


**Fig. 1 | Material characterization and performance assessment. a** High-resolution scanning electron microscope (SEM) images of BiOI and I-BiOI grown on carbon cloth. **b** High-resolution transmission electron microscopy (TEM) image of I-BiOI. **c** High-resolution I 3 d X-ray photoelectron spectroscopy (XPS) spectra for BiOI@CC and I-BiOI@CC. **d** Fourier transform infrared (FTIR) spectra of BiOI@CC and I-BiOI@CC. **e** Electrochemical impedance spectra (EIS) and **f** electrochemical surface area (ECSA) of BiOI@CC and I-BiOI@CC measured in the presence of acetaminophen (ACE). The dot-dashed lines in **f** are obtained through fitting with y = 1.94x + 8.96 for I-BiOI and y = 1.42x + 14.99 for BiOI. **g** ACE removal profiles by the electrocatalytic system over different anodes. **h** ACE and total organic carbon (TOC) removal efficiencies by the I-BiOI@CC under different applied potentials. **i** Comparison of removal kinetics ($k_{obs}$) of phenols, oxidant dosages, and polymerization selectivity between this study and the reported polymerization technologies by high-valent metal-oxo (HVMO) species and free radicals. **j** Electrocatalytic removal of ACE across different pH. **k** Effects of coexisting anions (5 mM) and humic acid with different concentrations on the removal efficiencies of ACE. Unless otherwise indicated, the experimental conditions are: 1.0 V vs. Ag/AgCl applied voltages, $[ACE]_0$ = 20 μM, $[pH]_0$ = 7.0 ± 0.1, using I-BiOI@CC anode, T = 298.15 K. Pollutant removal experiments were conducted in triplicate, and the obtained data with standard deviation (SD) less than 5%. Data are presented as mean values +/- SD for **g**, **h** and **j**, **k**.

an enlarged electrochemically active surface area for polymerization reaction. This enhancement aligns with the increased I loading in I-BiOI@CC revealed by XPS spectra, implying that the iodine species are the main active sites and their enhanced exposure markedly enhances material surface reactivity.

The electrocatalytic performance of the prepared anodes was assessed via ACE polymerization experiments. I-BiOI@CC exhibits enhanced ACE adsorption (9.2%, Figure S8a) compared to BiOI@CC (5.5%) because increased iodine sites enable stronger I···H–O interactions with ACE that promote interfacial PCET. As such, I-BiOI@CC achieves 91.4% of ACE removal at 1.0 V vs. Ag/AgCl within 10 min (Fig. 1g), significantly outperforming BiOI@CC (55.4%) and bare CC (10.1%), thereby evidencing the enhancement brought by I enrichment. Additionally, $I_2$@CC exhibits limited ACE removal (26.1%, Fig. S8b), suggesting that iodine enrichment within the BiOI framework, rather than iodine alone, enhances pollutant polymerization through offering abundant adsorption sites for phenols and reversible $I^-/I_3^-$ redox mediation. The disappearance of the excitation-emission-matrix (EEM) signal for the phenolic group (excitation 280–330 nm, emission 320–480 nm) in ACE solutions after treatment by I-BiOI@CC further verifies the efficient ACE removal (Fig. S9).

Figure S10a exemplifies that insufficient or excessive I loadings lead to suppressed performance, resulting from the limited iodine active sites and hindered charge transfer, respectively[21]. The declining ACE removal efficiencies with increasing ACE concentrations (Fig. S10b) further indicate that catalytic activity is governed by the availability of iodine active sites. Moreover, I-BiOI@CC synthesized at −0.1 vs. Ag/AgCl achieves the best performance in ACE removal (Fig. S11a). This is because the reduction peak for I-BiOI electrodeposition appears at 0 V vs. Ag/AgCl, and applying a potential 0.1 V

more negative provides the necessary overpotential to overcome activation barriers and sustain a high deposition rate (Fig. S11b). The I-BiOI@CC anodes prepared in 5 and 10 min exhibit similar performance with over 91% ACE removal, whereas the 2-min sample achieves less than 60% (Fig. S12a). SEM images exhibit that longer deposition leads to rougher surfaces with increased exposure of iodine sites (Figs. S12b–d), and 5 min is preferred considering energy effectiveness. Furthermore, I-BiOI@CC exhibits improved removal efficiencies for ACE and total organic carbon (TOC) with increasing applied voltages, attaining 87.2% TOC removal at 1.0 V vs. Ag/AgCl (Fig. 1h). Notably, a pronounced increase in ACE and TOC removal is observed at 0.8 V, corresponding to the onset potential for ACE oxidation at 0.65 V (Fig. S13a) and the significantly reduced resistance for charge transfer at 0.75 V (Fig. S13b).

Several tests were conducted to verify the occurrence of polymerization. The decreased current in the 10-cycle CV curves with 3 mM ACE reveals the passivation of I-BiOI@CC by polymerized products (Fig. S14), demonstrating that polymerization, rather than mineralization, dominates pollutant removal[29]. The non-detected $CO_2$ generation and negligible variations in inorganic carbon concentrations during ACE removal further confirm that mineralization is minimal (Fig. S15a). Notably, the electrocatalytic system using I-BiOI@CC achieves an impressive polymerization selectivity of 97.1%, as determined by measuring the mass fraction of phenolic pollutants converted into insoluble polymerized products adopting a tetrahydrofuran extraction method (Fig. S15b). In comparison with other polymerization systems (Fig. 1i and Table S1), the electrocatalytic system demonstrates significant advantages, including accelerated kinetics, exceptional polymerization selectivity, and the elimination of oxidant requirements.

Regarding potential interference from water matrices, I-BiOI@CC maintains consistent performance across pH 5–9 (Fig. 1j) that is not affected by its surface Zeta potential (Fig. S16). Common anions ($HCO_3^-$, $Cl^-$, $NO_3^-$, and $H_2PO_4^{2-}$) and varying concentrations of humic acid (a representative of natural organic matter) exhibit negligible effects on ACE removal (Fig. 1k), demonstrating the strong resistance of the electrochemical system to external interference. This exceptional selectivity is primarily attributed to the strong affinity of iodine species towards phenolic hydroxyl groups for forming hydrogen bonds[21,30], facilitating selective adsorption for subsequent polymerization.

## Mechanistic insights into PCET-driven polymerization

Scavenging tests were conducted to identify the reactive species involved in ACE polymerization and reveal the roles of iodine sites (Fig. 2a). Methanol addition has a negligible effect on ACE removal, excluding the participation of $^{\bullet}OH$[31]. In contrast, ferulic acid (FA), an antioxidant for quenching phenoxyl radicals (Fig. S17), dramatically suppresses ACE removal by 79.3%, suggesting that phenoxyl radicals are predominant intermediates in ACE polymerization[13]. Quenching the iodine sites with $AgNO_3$ inhibits 79.9% of ACE removal, confirming the crucial role of iodine sites in driving ACE polymerization. Consistently, the inefficient ACE removal by BiOF@CC, BiOBr@CC, and BiOCl@CC (Fig. S18), along with negligible changes in the Bi XPS spectra after reaction (Fig. S19), provides evidence that I, rather than Bi and O, serves as the primary active site.

The oxidation of 2,2-azino-bis-3-ethylbenzothiazoline-6-sulfonic acid (ABTS) was performed to exclude the involvement of strong oxidative species during electrocatalytic polymerization[32]. Figure 2b shows that I-BiOI@CC efficiently transforms ABTS to $ABTS^{\bullet+}$ (95.4%) with negligible $ABTS_{ox}$ formation, demonstrating that the electrocatalytic system highly selectively oxidizes the substrate to organic radicals while suppressing over-oxidation. The phenoxyl radical generation was verified through electron paramagnetic resonance (EPR) and liquid chromatography-mass spectrometry (LC-MS) analysis. Using 5,5-dimethyl-1-pyrroline N-oxide (DMPO) as the spin-trapping agent (Fig. S20)[33], a strong signal with a spectrum width of 40.5 G for phenoxyl radical is detected (Fig. 2c). This signal is substantially diminished with the addition of FA, confirming phenoxyl radical formation during ACE polymerization. The existence of phenoxyl radical is further validated through trapping experiment using (2,2,6,6-tetramethyl piperidine-1-yl) oxyl (TEMPO)[34]. The extracted ion chromatogram (EIC) exhibits peaks at *m/z* 150.1, 156.1, and 307.2, corresponding to the parent ions of ACE and TEMPO, and the cross-coupling product (TEMPO–PhO), respectively, demonstrating the oxidation of ACE to phenoxyl radical (Fig. 2d). Therefore, the electrocatalytic system selectively oxidizes ACE to generate phenoxyl radical for polymerization, initiated at iodine active sites.

Various investigations were conducted to elucidate that the electrocatalytic pollutant polymerization proceeds through PCET. The Nernstian shift analysis was conducted using phenol as a chemical probe across pH 6–10 (Fig. 2e), which reveals a systematic negative shift in oxidation potentials with increasing alkalinity, indicating involvement of proton transfer[18]. The slope of oxidation potentials versus pH (inset of Fig. 2e) is determined as 57.2 mV $pH^{-1}$ ($R^2$ = 0.9944), close to the theoretical Nernstian value (59.2 mV $pH^{-1}$), with an implication that the polymerization proceeds via a coupled one-electron/one-proton pathway. Although oxidation potentials shift with pH, the 1.0 V vs. Ag/AgCl applied voltage is significantly higher than the thermodynamic threshold for PCET across, thus the electrocatalytic system maintains high polymerization efficiency across pH 5–9. Moreover, the negligible effect of quenching phenoxenium ions on ACE removal (Fig. S21) suggests that direct oxidation transfer (two-electron, one-proton coupled transfer) is not involved in electrocatalytic polymerization[9].

High-resolution I 3 d XPS spectra of I-BiOI after electrocatalytic reactions (Fig. 2f) display a higher ratio of $I^-$ (79.7%) in the presence of ACE compared to without ACE (67.6%), demonstrating substantial charge transfer from ACE to iodine (reducing $I_3^-$ to $I^-$) and further confirming iodine species as main active sites. Additionally, CV curves (Fig. 2g) reveal that the oxidation of $I^-$ to $I_3^-$ in I-BiOI@CC diminishes while the reduction of $I_3^-$ to $I^-$ strengthens with the presence of ACE, further evidencing the oriented charge transfer from ACE to I-BiOI@CC[35]. This result indicates that $I^-/I_3^-$ redox pairs serve as the electron shuttle during PCET: $I^-$ is oxidized to $I_3^-$ ($3I^- \rightarrow I_3^-$) under anodic polarization to generate the electron-deficient iodine species to facilitate interaction with phenolic pollutants, while $I_3^-$ accepts electrons from the phenolic pollutant ($I_3^- \rightarrow 3I^-$) to induce phenoxyl radical formation. Such reversible redox transitions ($3I^- \leftrightarrows I_3^-$) also stabilize surface charge migration, which constrains pollutant over-oxidation and enhances polymerization selectivity[36]. The in-situ Raman spectra (Fig. S22 exhibit two peaks at 110.8 and 153.4 $cm^{-1}$ for lattice Bi–I vibration and surface $I^-$ species of I-BiOI@CC at 0 min. With the reaction proceeding, an additional peak at 182.6 $cm^{-1}$ assigned to $I_3^-$ appears, evidencing the reversible $3I^- \rightleftharpoons I_3^-$ redox transition to mediate charge transfer during phenol polymerization. Moreover, the increasing O–H band (3200–3600 $cm^{-1}$) indicates interaction between phenolic hydroxyl groups and I-BiOI and accumulation. These results collectively demonstrate iodine active sites synergistically strengthen pollutant-material interaction and mediate electron transfer to promote phenol polymerization. Furthermore, according to the removal profiles of phenol and the deuterated phenols (Fig. S23), the electrocatalytic system displays a high kinetic isotope effect (KIE) of 4.92 (Fig. 2h) upon deuteration of phenolic hydroxyl groups ($C_6D_5OD$), whereas the value is close to 1 for $C_6D_5OH$ (1.12). This finding evinces that the pollutant polymerization proceeds with PCET and reveals that I-BiOI specifically interacts with the phenolic hydroxyl group to induce phenoxyl radical generation[18].

Density functional theory (DFT) calculations further clarify the mechanisms underlying electrocatalytic polymerization. Density of states (DOS) analyses (Fig. 2i) reveal that I enrichment induces mid-gap

https://doi.org/10.1038/s41467-026-74349-6

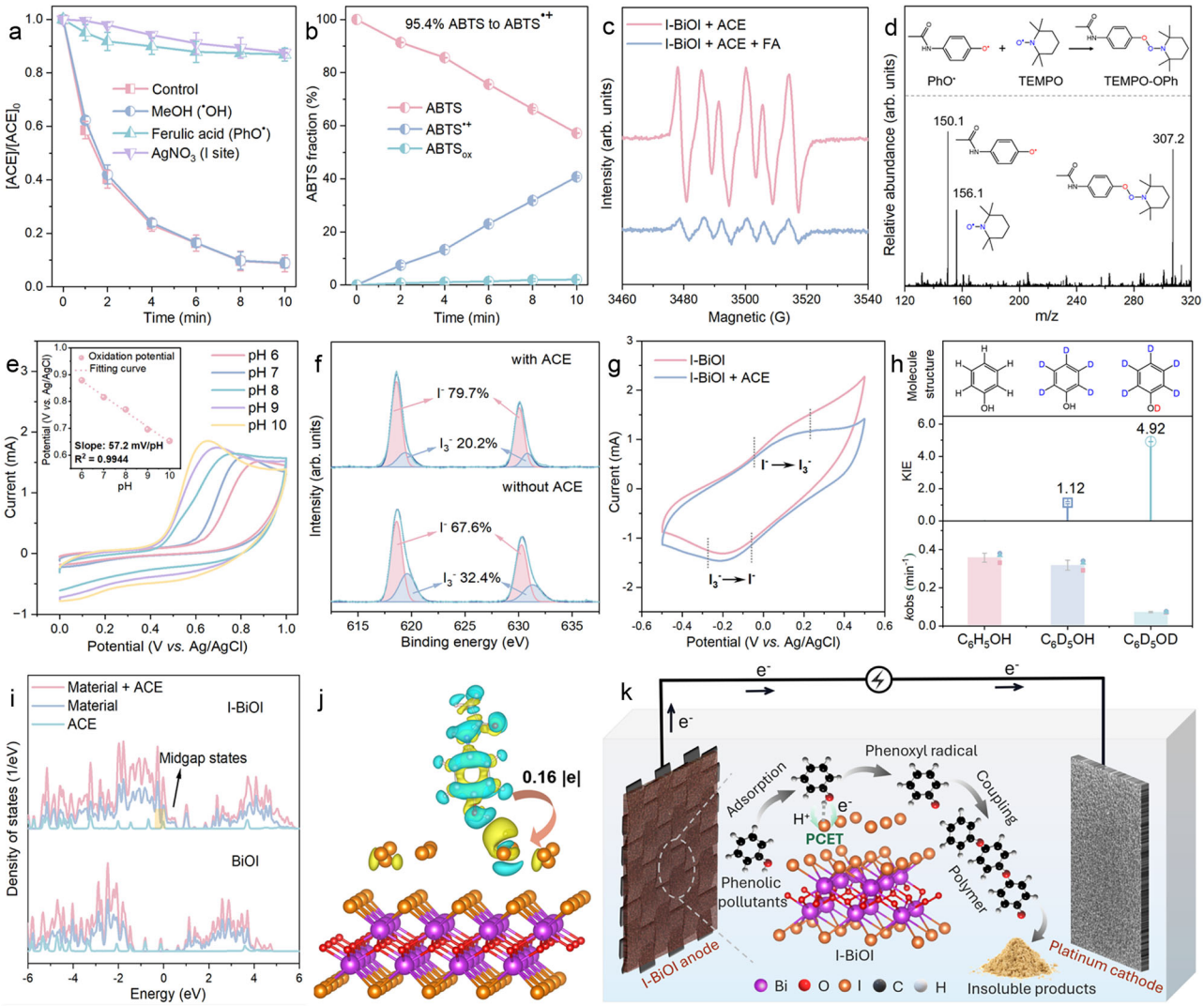


**Fig. 2 | Mechanistic insights into electrocatalytic polymerization via PCET.** **a** Electrocatalytic removal of ACE (20 μM) by the I-BiOI@CC anode with the addition of various scavengers (5 mM). **b** Electrocatalytic conversion of 2,2′-azino-bis(3-ethylbenzothiazoline-6-sulfonic acid (ABTS) to $ABTS^{\bullet+}$ and $ABTS_{ox}$ over the I-BiOI@CC anode. **c** Electron paramagnetic resonance (EPR) spectra of phenolic radicals during ACE removal over the I-BiOI@CC anode with and without the addition of ferulic acid (FA). **d** Liquid chromatography–mass spectrometry (LC-MS) spectra and reaction mechanism for the trapping of phenoxyl radical (PhO•) using TEMPO as a probe. **e** Nernstian shift analysis of phenol oxidation across pH 6–10. The insert shows the linear correlation of oxidation potential vs. pH, and the dot-dashed line is obtained through fitting with $y = -0.0572x + 1.22$. **f** High-resolution XPS spectra of I 3 d for used I-BiOI@CC anodes in the electrocatalytic system with and without ACE. **g** Cyclic voltammetry (CV) of the I-BiOI@CC anode with and without ACE. **h** Kinetic isotope effect (KIE) analysis for oxidation of phenol (10 μM) with H/D by I-BiOI@CC anode. **i** Density of states (DOS) of BiOI and I-BiOI before and after the introduction of ACE. **j** Charge density difference of the optimized I-BiOI/ACE configuration, with yellow and cyan indicating charge accumulation and charge depletion, respectively. **k** Proposed mechanisms of electrocatalytic ACE polymerization through PCET over the I-BiOI@CC anode. Unless otherwise indicated, the experimental conditions are: 1.0 V vs. Ag/AgCl applied voltages, $[ACE]_0 = 20$ μM, $[ABTS]_0 = 20$ μM, $[phenol]_0 = 20$ μM, $[pH]_0 = 7.0 \pm 0.1$, using I-BiOI@CC anode, $T = 298.15$ K. Pollutant removal and probe experiments were conducted in triplicate, and the obtained data with SD less than 5%. Data are presented as mean values +/- SD for (**a**, **b**, **h**).

states near the Fermi level of I-BiOI, which facilitates charge transfer, while ACE adsorption significantly strengthens these localized electronic states, suggesting strong interfacial orbital overlap at the interface[37]. In comparison, BiOI exhibits a cleaner band structure with limited charge delocalization, consequently there is only a minor change in electronic states upon ACE adsorption. The adsorption of ACE on BiOI and I-BiOI likely occurs through hydrogen bonding at the phenolic hydroxyl group (–OH) and its *ortho* C–H sites, and the corresponding adsorption configurations are shown in Fig. S24. Quantitative analysis (Table S2) indicates that BiOI exhibits a stronger affinity towards the *ortho* C–H ($E_{ads} = -0.21$ eV, $L_{I-H} = 3.06$ Å) than the phenolic –OH ($E_{ads} = -0.18$ eV, $L_{I-H} = 3.19$ Å), which is attributed to the higher electron density around the aromatic ring and the orbital overlap between Bi 6p orbitals and *ortho* C–H bond[38]. In contrast, I-BiOI preferentially adsorbs ACE through hydrogen bonding at the phenolic –OH site ($E_{ads} = -0.28$ eV, $L_{I-H} = 2.86$ Å) than the *ortho* C–H site ($E_{ads} = -0.21$ eV, $L_{I-H} = 2.90$ Å), owing to the enriched surface iodine sites that tend to form a hydrogen bond with the phenolic –OH[30]. This selective interaction of I-BiOI towards phenolic –OH is corroborated by the spin density diagrams of phenoxyl radical (Fig. S25), where the confined state on I-BiOI displays strong electron localization at the interface, whereas the isolated state shows delocalization at the C aromatic atoms.

Based on the optimized adsorption with I-BiOI towards phenolic –OH site, charge density difference was obtained to study the charge transfer between I-BiOI and ACE (Fig. 2j). The interface of I-BiOI/ACE configuration exhibits significant electronic reconfiguration, with electron depletion at the phenolic –OH moiety and electron

accumulation at the iodine sites of I-BiOI, indicating directional charge transfer from ACE to I-BiOI. Bader charge analysis quantifies approximately 0.16|e| transfer from ACE to the I-BiOI surface, and this solid interfacial electronic modulation can facilitate phenoxyl radical generation. In contrast, BiOI/ACE configuration (Fig. S26) shows negligible charge redistribution with limited electron transfer (0.02 |e|). The findings of DFT calculations indicate that I enrichment alters the adsorption behavior of ACE on I-BiOI and efficiently regulates the local electronic structure of ACE upon adsorption to promote charge transfer, which in turn facilitates the PCET-driven electrocatalytic polymerization.

Figure 2k schematically illustrates the oxidant-free electrocatalytic polymerization mechanisms. The I-BiOI@CC anode selectively adsorbs phenolic pollutants via hydrogen bond to iodine (H···I), followed by anodic oxidation to induce PCET, generating phenoxyl radicals. Meanwhile, the mild applied voltage is below the threshold for ·OH generation, suppressing pollutant over-oxidation. Subsequently, phenoxyl radicals self-couple to form insoluble polymers, achieving efficient pollutant removal.

## Polymerization routes of ACE by I-BiOI@CC

The ACE molecular transformation during electrocatalytic polymerization was analyzed using various techniques. The interaction of ACE with I-BiOI during polymerization was first probed using the in situ FTIR spectrometer (Fig. 3a). Distinct variations in vibrational features over reaction time can be observed, attributed to the ACE structural transformation on the I-BiOI surface during electrocatalytic polymerization. Notably, the gradual increases of $\nu_{O-H}$ at 3288 $cm^{-1}$ and $\nu_{C=C}$ (aromatic) at 1635 $cm^{-1}$ reflect the accumulated adsorption of ACE molecules on I-BiOI surface through the interaction with phenolic -OH to form hydrogen bond to iodine (I···H–O–Ph)[39]. Such a phenolic –OH oriented adsorption of ACE by I-BiOI is consistent with the KIE results and DFT calculation. The formed I···H can facilitate electron transfer from ACE to I-BiOI, promoting ACE oxidation to generate phenoxyl radical via the PCET pathway. The elemental mapping of used I-BiOI exhibits distinct C signal, suggesting the interfacial interaction between the material and ACE (Fig. S27). Additionally, a weak $\nu_{C-O-C}$ peak located at 1205 $cm^{-1}$ matches the observation of C–O–C peaks in O 1 s (530.9 eV, Fig. S28a) and C 1 s (285.9 eV, Fig. S28b) XPS spectra of the used I-BiOI@CC anode, which demonstrates the occurrence of C–O coupling during ACE polymerization. The presence of O–H and C = O in the high-resolution XPS spectra of O1s and C1s for the used I-BiOI@CC again validates the oriented ACE adsorption and its subsequent polymerization on the I-BiOI surface. The mass weight of the collected polymerized products was then revealed by time-of-flight mass spectrometry (TOF-MS) using tetrahydrofuran as the solvent (Fig. 3b). Multiple polymerized products with repeated units of *m/z* = 149.0–149.2 corresponding with the ACE polymers are observed, confirming the successful electrocatalytic polymerization of ACE.

The ACE polymerization routes were further deduced by integrating DFT calculations and mass spectrometry analysis. As revealed by HOMO and nucleophilic Fukui functions ($f^-$), the oxygen atom of the phenolic hydroxyl group possesses the greatest electron density and the highest $f^-$ value (Table S3), while the carbon atom adjacent to the hydroxyl group exhibits the second-highest reactivity (Fig. 3c). Moreover, Laplacian bond order analysis[40] illustrates that the O7–H16 and C3–O7 have the lowest and highest bond orders, respectively, and the C–H bonds display comparable bond orders. Hence, ACE oxidation to form phenoxyl radicals on the phenolic hydroxyl group and the adjacent carbon atom is more favorable than molecule destruction. These radicals can undergo polymerization through two potential routes (Fig. 3d): route I involves the *ortho* C–O coupling to generate poly(-oxyphenylene) segments with oxygen-bridged linkages; route II proceeds with *ortho* C–C coupling to form carbon-carbon bonded polymers with high conjugation but low stability. Furthermore, LC-MS analysis offers clear *m/z* information for the polymerization intermediates of ACE (Fig. S29a–c), including dimer, trimer, and tetramer. Nevertheless, the shared *m/z* values of the C–O and C–C coupling products make it difficult to determine which route is predominant.

Gibbs free energy variations during ACE polymerization were further calculated to reveal the coupling energies, thereby determining the preferred reaction route. For the *ortho* C–O coupling (route I, Fig. 3e), ACE undergoes PCET to form monomer radicals on the phenolic hydroxyl group (0.96 eV) and the adjacent carbon atom (2.37 eV), and the coupling of these radicals results in the formation of a dimer with a total thermodynamic barrier of 3.33 eV. The resulting dimer can be further oxidized via PCET to produce dimer radicals that couple with monomer radicals to produce a trimer (2.99–3.03 eV), while the tetramer is formed through similar reactions with thermodynamic barriers of 3.17–3.33 eV. In contrast, *ortho* C–C coupling (route II, Fig. 3f) proceeds through a substantially higher thermodynamic barrier of 4.73 eV for forming the dimer, mainly due to the elevated energy required for the formation of the monomer radical on the adjacent carbon atom (2.37 eV). The subsequent formation of trimer and tetramer along this route requires a similar thermodynamic barrier of 4.73–4.74 eV, implying that route II is thermodynamically hindered and difficult to proceed. These thermodynamic trends correlate with the stronger affinity of I-BiOI towards the phenolic –OH compared with the adjacent C–H, evidenced by higher adsorption energy and shorter $L_{I-H}$ (Fig. S24c, d). The lower KIE of I-BiOI@CC anode for $C_6D_5OH$ (1.12, Fig. 2h) compared to $C_6D_5OD$ (4.92) also verifies the priority of PECT occurring at the phenolic –OH site of ACE. Additionally, FTIR and XPS analyses of the polymerized products (Fig. S30) confirm polymer formation, evidenced by intensive C–O–C stretching (1207 $cm^{-1}$), aromatic ring signals (1450–1480 and 820 $cm^{-1}$), and a significant C–O–C peak in the C 1 s spectrum. These results verify that C–O–C formed by *ortho* C–O coupling is a key functional group in the polymerized products. Collectively, the integrated theoretical-experimental analyses reveal that ACE polymerization via PCET primarily follows the thermodynamically and kinetically favored *ortho* C–O coupling route.

Frontier orbital theory calculations were performed to identify the energetically favorable ACE polymerization route[41]. Theoretically, electron transfer occurs from the HOMO of organic compounds to that of the electrocatalyst, initiating oxidation. Accordingly, the HOMO levels of the ACE polymerization intermediates determine the accessibility for driving PCET to form phenoxyl radicals for sequential reactions. For route I, the dimer, trimer, and tetramer intermediates through *ortho* C–O coupling (Fig. S31 for detailed electronic structures) exhibit a slight upward of HOMO levels compared to ACE, demonstrating enhanced electron-donating capacities with higher reactivity to proceed PCET (Fig. 3g). In contrast, the HOMO levels of the intermediates formed in route II via *ortho* C–C coupling (Fig. S32 for detailed electronic structures) show a slight decrease or minor change, which raises the thermodynamic barrier for PCET and makes it unfavorable (Fig. 3h). These results further evidence that the *ortho* C–O coupling is the major route of electrocatalytic polymerization.

## Structure-reactivity correlation of pollutant polymerization

The structure-kinetics relationships underlying electrocatalytic polymerization were elucidated using 10 phenolic pollutants with distinct functional groups. Except for 4-nitrophenol (4-NP, with nitro–), I-BiOI@CC anode achieves efficient removal (>80% in 10 min) of other phenols (with amino–, methoxyl–, formyl–, methyl–, etc., Figure S33) with observed rate constants ($k_{obs}$) ranging from 2.08 to 0.21 $min^{-1}$ (Fig. 4a). The Marcus-Hush analysis was employed to determine the involvement of PCET during electrocatalytic polymerization of different phenolic pollutants[18]. The <-1/51 meV slope in the correlation between -ln $k_{obs}$ and free energy of phenolic pollutants (ΔG, determined based on oxidation peaks of pollutants, Fig. S34 and Table S4)

https://doi.org/10.1038/s41467-026-74349-6

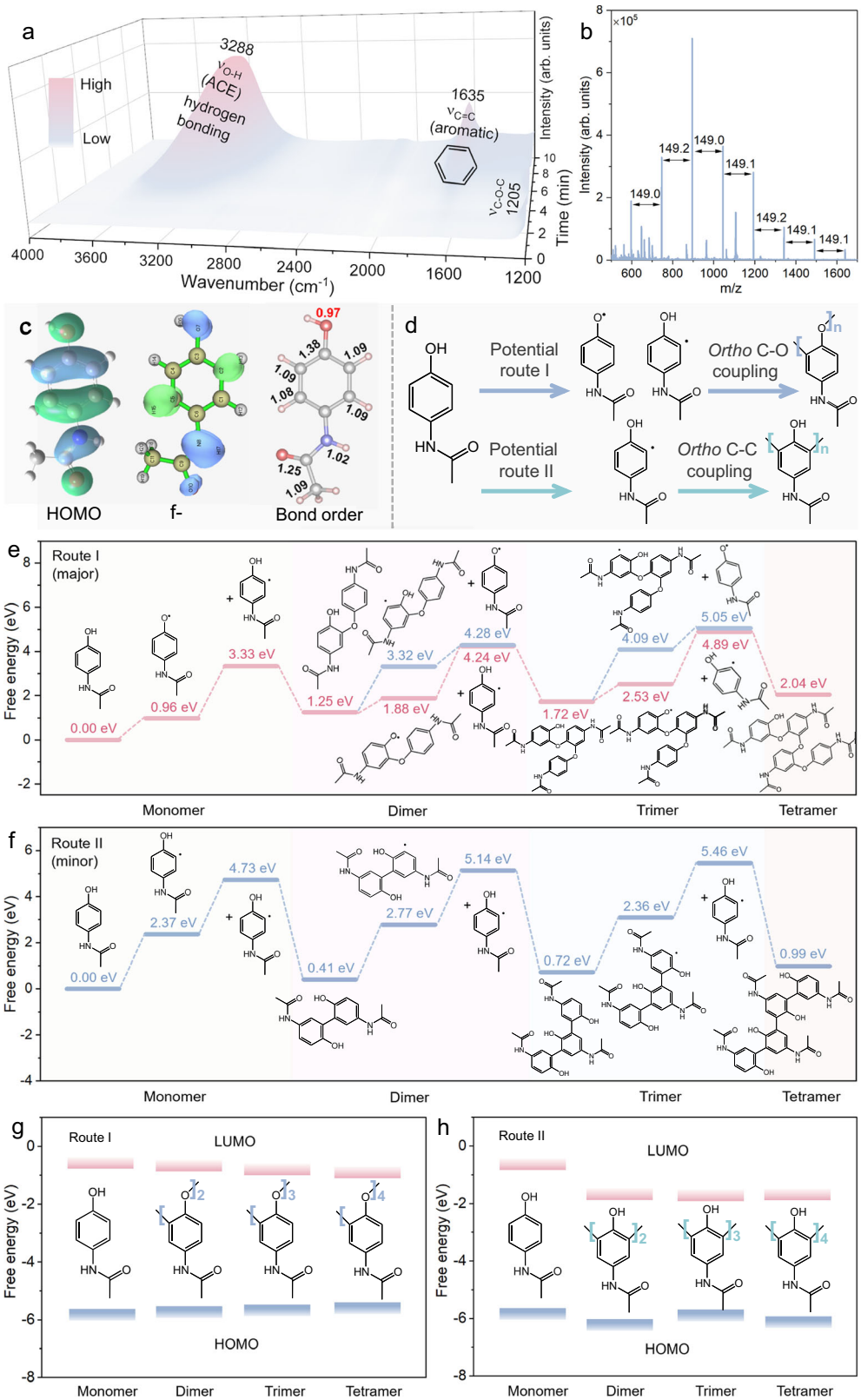


**Fig. 3 | ACE polymerization routes and thermodynamic analysis. a** Time-dependent in situ FTIR spectra of I-BiOI@CC anode during electrocatalytic ACE polymerization. **b** Time of flight mass spectrometry (TOF-MS) spectrum of the collected polymerized products using tetrahydrofuran as the solvent. **c** Highest occupied molecular orbital (HOMO), Fukui reactivity function ($f^-$), and Laplacian bond order of ACE. **d** Two potential routes of ACE polymerization, including *ortho* C–O coupling and *ortho* C–C coupling. Gibbs free energy variations of ACE polymerization through **e** *ortho* C–O coupling and **f** *ortho* C–C coupling. **g** HOMO and lowest unoccupied molecular orbital (LUMO) energy levels of ACE polymerization intermediates via the *ortho* C-O polymerization route and **h** *ortho* C–C polymerization route.

https://doi.org/10.1038/s41467-026-74349-6

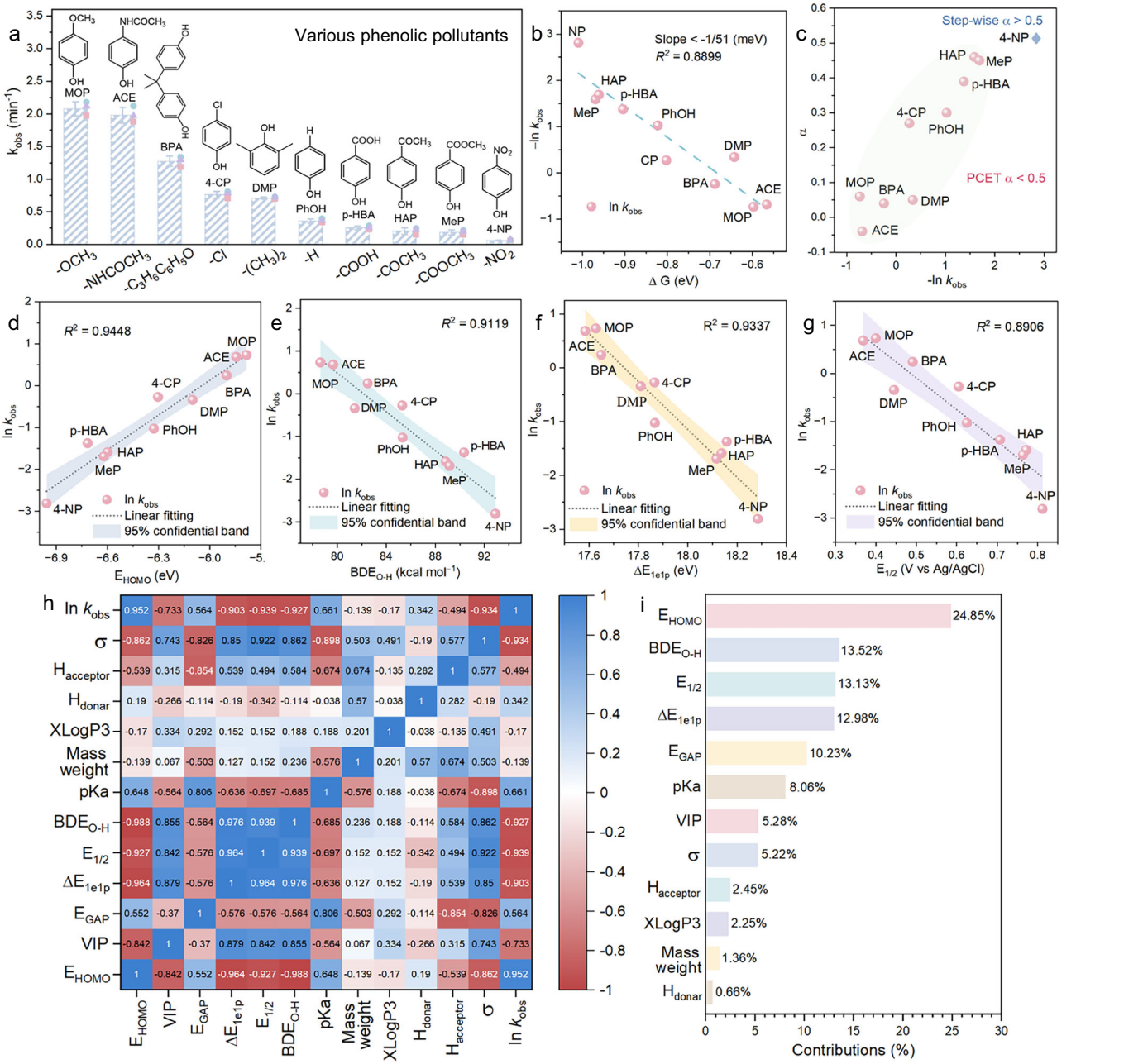


**Fig. 4 | Structure–reactivity correlations and quantitative analysis for electrocatalytic polymerization of phenolic pollutants. a** Observed rate constants ($k_{obs}$) for electrocatalytic polymerization of diverse phenolic pollutants by I-BiOI@CC anode. The used organic pollutants include acetaminophen (ACE), phenol (PhOH), 2,6-dimethylphenol (DMP), 4-hydroxybenzoic acid (HBAc), 4-chlorophenol (4-CP), 4-nitrophenol (4-NP), bisphenol A (BPA), 4-hydroxyphenylacetaldehyde (HAP), 4-methoxyphenol (MeP), and methylparaben (MHB). Relationship between the logarithmic rate constant (ln $k_{obs}$) and **b** free energy (ΔG) and **c** electron transfer coefficient (α) based on the Marcus-Hush analysis. Linear regression analysis between the ln $k_{obs}$ and several key molecular descriptors: **d** energy levels of HOMO ($E_{HOMO}$), **e** dissociation energies of O-H bond ($BDE_{O-H}$), **f** energy changes with losing one electron and one proton ($\Delta E_{1e1p}$), and **g** oxidation potentials ($E_{1/2}$). The colored regions in Fig. 4b-g represent 95% confidence intervals for linear fittings, and $R^2$ values indicate the extent of correlation between ln $k_{obs}$ and the molecular descriptors. The dot-dashed lines in (**b**, **d**–**g**) are obtained through fitting with y = -6.61x − 4.52 for (**b**), y = 2.76x + 16.72 for (**d**), y = -0.23x + 18.70 for (**e**), y = -4.45x + 78.92 for (**f**), and y = -6.61x + 3.22 for (**g**), respectively. **h** Correlation heatmap of various molecular descriptors and ln $k_{obs}$ based on the Spearman model. **i** Relative contributions of different molecular descriptors to the kinetics for polymerization of phenolic pollutants based on the mean decrease impurity (MDI) model. The molecular descriptors include $E_{HOMO}$, $BDE_{O-H}$, $E_{1/2}$, $\Delta E_{1e1p}$, vertical ionization potentials (VIP), Hammett constants (σ), mass weight, hydrophobic characteristics (XLogP3), acid dissociation constant (*pKa*), H as donor ($H_{donor}$), and H as acceptor ($Ha_{cceptor}$). Unless otherwise indicated, the experimental conditions are: 1.0 V vs. Ag/AgCl applied voltages, $[phenolic\ pollutants]_0$ = 10 μM, $[pH]_0$ = 7.0 ± 0.1, using I-BiOI@CC anode, $T$ = 298.15 K. Pollutant removal experiments were conducted in triplicate, and the obtained data with SD less than 5%. Data are presented as mean values +/- SD for (**a**, **d**–**g**).

suggests the dependence of rate constant on ΔG, which indicates the energetically coupled proton and electron transfer, and higher free energy promoting the PCET (Fig. 4b). Additionally, most phenolic pollutants fall within an electron transfer coefficient (α, Table S5) < 0.5 that reflects the concerted PCET, while 4-NP deviates, showing a stepwise proton-electron transfer process (Fig. 4c). This is attributed to the electron-withdrawing nature of the para-nitro group on 4-NP, which facilitates the formation of a high-energy radical cation intermediate

($ArOH^{\bullet+}$) before proton loss, a step thermodynamically unfavorable for polymerization, resulting in hindered polymerization kinetics.

Linear regression analysis between molecular orbital and thermodynamic parameters (obtained from experimental investigation and DFT calculations) and ln $k_{obs}$ was established to study the effects of pollutant properties on polymerization rate constants. For frontier molecular orbit energies, the correlation analysis exhibits a strongly positive linear ($R^2 = 0.9448$, Fig. 4d) relationship between ln $k_{obs}$ and the highest occupied molecular orbital ($E_{HOMO}$, obtained via DFT calculation, Fig. S35) values, attributed to compounds with higher $E_{HOMO}$ processing greater electron-donating capacity that tend to lose electrons to promote PCET. In contrast, the ln $k_{obs}$ shows an inverse linear with O–H bond dissociation energy ($BDE_{O-H}$, Fig. 4e, $R^2 = 0.9119$), as a weaker phenolic O–H bond benefits proton transfer during oxidation to form phenoxyl radical. Similarly, two additional inverse relationships are observed in in Fig. 4f ($R^2 = 0.9337$) for energy change with losing one electron and one proton ($\Delta E_{1e1p}$) and Fig. 4g ($R^2 = 0.8906$) for half-wave potentials ($E_{1/2}$, obtained from experimental measurement, Fig. S34), implying that phenolic pollutants with less energy variations during coupled proton and electron and lower oxidation potential are more likely to undergo PCET, respectively. The vertical ionization potentials (VIP, Fig. S36a, R2 = 0.7281) and Hammett constants (σ, Fig. S36b, R2 = 0.8242) present low $R^2$ values with several data points deviated from the 95% confidence band. This relatively weak correlation to the PCET mechanism may be attributed to the neglect of effects from proton transfer[34]. Overall, these results indicate that the polymerization via PCET is kinetically regulated by the coupled dynamics of proton and electron transfer of phenolic pollutants.

Although linear regression analysis effectively describes pollutant polymerization kinetics for individual parameters, it fails to establish the intrinsic relationships among multiple parameters[42]; thus, the machine learning approaches were used to reveal the collective effects of pollutant properties. The correlation heatmap (Fig. 4h) provides a quantitative description of interdependence among 12 descriptors (Table S6) based on Spearman model, and their connections with ln $k_{obs}$. The chemical significance across independent descriptors is elucidated by their correlation: $BDE_{O-H}$, $\Delta E_{1e1p}$, and $E_{1/2}$ illustrate strong intercorrelations ($\rho > 0.94$), as they share dependence on energies for proton and electron transfer; while $E_{HOMO}$ exhibits inverse relationship ($\rho < -0.92$) to $BDE_{O-H}$, $E_{1/2}$, and $\Delta E_{1e1p}$, implying that phenolic pollutants with higher $E_{HOMO}$ are more prone to phenolic O–H bond broken, coupled transfer of one electron and proton, and oxidation, respectively. Notably, ln $k_{obs}$ demonstrates a marked positive correlation with $E_{HOMO}$ ($\rho = 0.952$), while presenting strong negative correlations with $BDE_{O-H}$ ($\rho = -0.927$), $E_{1/2}$ ($\rho = -0.939$) and $\Delta E_{1e1p}$ ($\rho = -0.903$). In contrast, the hydrophobic (XlogP3) and steric (mass weight) descriptors exhibit insignificant correlations with $k_{obs}$. The moderately hydrophilic surface (~77°, Fig. S3b) of I-BiOI renders the hydrophobicity of phenolic pollutants a negligible factor for polymerization. Furthermore, the relative contributions of the descriptors to pollutant polymerization were evaluated using the mean decrease impurity (MDI) model (Fig. 4i). $E_{HOMO}$ exhibits the highest contribution (24.85%), followed by $BDE_{O-H}$ (13.52%), $E_{1/2}$ (13.13%), and $\Delta E_{1e1p}$ (12.98%), suggesting that polymerization kinetics are predominantly governed by the electron- and proton-transfer processes with greater electron-donating capacity and weaker O–H favoring PCET. For comparison, the descriptors associated with steric (mass weight, 1.36%), hydrophobicity (XLogP3, 2.25%), and molecular polarity ($pK_a$, 8.06%) contribute insignificantly. This mechanistic framework correlating pollutant properties to polymerization kinetics provides predictive insight into their oxidation behaviors.

### Sustainability, toxicity, and practicality assessment

The sustainability of electrocatalytic polymerization was evaluated in terms of energy consumption, costs, and life cycle assessment (LCA). Electrocatalytic ACE polymerization demonstrates an exceptional TOC removal of 87.2% (Fig. 5a and Table S7), outperforming mineralization-oriented electrocatalytic and photoelectrocatalytic systems (20–83%). It requires only 2.93 kWh/kg TOC removal (calculated from recorded current in Fig. S37[43]), which is 2–4 orders of magnitude lower than mineralization-oriented systems. This remarkable energy efficiency is attributed to the low charge transfer required for PCET-driven polymerization compared to conventional mineralization-oriented processes[5–7]. Consistent with this, electrochemical polymerization demonstrates a significantly low operational cost of $0.3/kg TOC removal, which is 30–50 times lower than PMS-based processes (Fig. 5b). The potential impacts of the electrocatalytic system using different anodes and the conventional Fenton process for wastewater treatment were compared using life cycle assessment (LCA). The LCA was conducted considering the whole life cycle, including catalyst preparation, wastewater treatment, catalyst reuse, and recovery of the polymerized products. The input and output materials and energy required for treating wastewater containing 1 kg ACE are listed in Table S8–11. Compared to the Fenton process (300.53 kg $CO_2$ eq) and other anodes (CC 231.82 kg $CO_2$ eq, BiOI@CC 65.62 kg $CO_2$ eq), I-BiOI@CC (42.78 kg $CO_2$ eq) evinces the lowest carbon footprint (Fig. S38), benefiting from its outperforming polymerization efficiency, mild applied potential for wastewater, and oxidant-free nature. Notably, the LCA comparison (Fig. 5c) reveals that I-BiOI@CC anode consistently exhibits the lowest environmental burdens across the 18 indicator categories for human health, aquatic ecology, terrestrial ecology, resources, and atmospheric domains. Overall, the electrocatalytic system using I-BiOI@CC demonstrates significantly improved sustainability and resource efficiency during wastewater treatment..

The biotoxicity of I-BiOI@CC for water treatment was evaluated through zebrafish embryo assays. Exposure to ACE and BiOI@CC treated ACE solutions causes 100% and 61.2% mortality during 96-h incubation (Fig. 5d), respectively, leading to embryonic lethality within 48 h of development (Fig. 5e). In contrast, I-BiOI@CC treatment and material leaching group exhibit negligible biotoxicity with comparable survival rates to blank and healthy development of embryos to fries. In terms of practicality assessment, the I-BiOI@CC achieves higher than 90% ACE removal from different kinds of water (Fig. 5f), which verifies the wide applicability of electrocatalytic polymerization. Notably, it sustains excellent performance in real wastewater (after secondary treatment, detailed water characteristics provided in Table S12), demonstrating strong resistance to complex matrix interference. Moreover, the continuous-flow operation (the reactor is provided in Fig. S39) was performed for the simultaneous removal of ACE, BPA, PhOH, and HAP. The I-BiOI@CC anode demonstrates outstanding performance, achieving high removal efficiencies of multiple phenols with over 94% COD removal during 72 h of continuous operation with a hydraulic retention time of 10 min (Fig. 5g). I-BiOI@CC also exhibits excellent stability with iodine and bismuth leaching below 0.1 ppm throughout the continuous-flow operation (Fig. S40), which is attributed to the mild applied potential that lies below the thermodynamic threshold for material self-oxidation. *Vibrio fischeri* test reveals a rapid decline in the biotoxicity from over 70% inhibition for the wastewater influent to below 10% inhibition for the treated effluent in the continuous-flow operation, further ensuring ecological safety (Fig. 5h). The exceptional performance of I-BiOI@CC in continuous-flow operation further emphasizes its strong application potential.

A simple regeneration approach is developed to restore the activity of the used I-BiOI@CC anode (after continuous-flow operation) by soaking it in the disposed electrolyte from its synthesis by stirring for 30 min. The electrolyte contains ethanol, iodide ions, and acidity, enabling the effective removal of polymerized products and reconstruction of iodine active sites. Figure S41 shows that the regenerated I-BiOI@CC anode achieves over 96% ACE removal across the 4-cycling tests, and it also attains an increased ECSA (2.1 mF $cm^{-2}$, Fig. S42) compared to the used I-BiOI@CC (1.5 mF $cm^{-2}$), validating its

https://doi.org/10.1038/s41467-026-74349-6

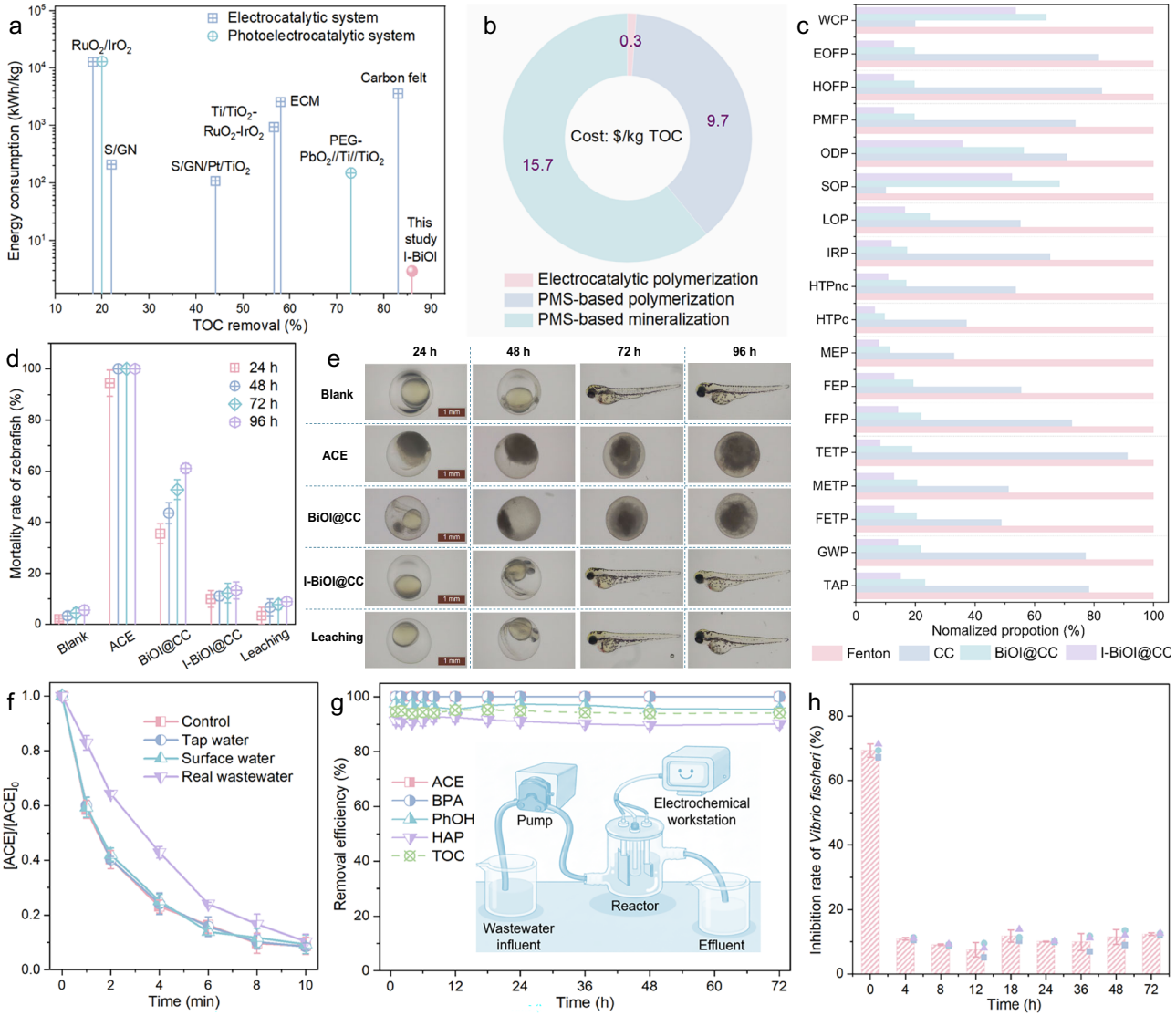


**Fig. 5 | Sustainability and practicality assessment of electrocatalytic polymerization over I-BiOI@CC anode. a** Comparison of TOC removal efficiency and energy consumption during ACE removal among electrocatalytic polymerization and mineralization-oriented electrocatalytic and photoelectrocatalytic systems. Detailed information is provided in Table S7 supporting by references [13–19] in the supplementary information. **b** Operational cost analysis for removal of phenolic pollutants over peroxymonosulfate (PMS)-based mineralization, PMS-based polymerization, and electrocatalytic polymerization. **c** Comparison of environmental impact for treating wastewater containing 1 kg of ACE by conventional Fenton process and electrocatalytic system with different anodes across 18 indicator categories in human health, aquatic ecology, terrestrial ecology, resources, and atmospheric domains. Terrestrial acidification potential (TAP), global warming potential (GWP), freshwater ecotoxicity potential (FETP), marine ecotoxicity potential (METP), terrestrial ecotoxicity potential (TETP), fossil fuel potential (FFP), freshwater eutrophication potential (FEP), marine eutrophication potential (MEP), human toxicity potential: carcinogenic (HTPc), human toxicity potential: non-carcinogenic (HTPnc), ionising radiation potential (IRP), agricultural land occupation (LOP), surplus ore potential (SOP), ozone depletion potential (ODP), particulate matter formation potential (PMFP), photochemical oxidant formation potential: humans (HOFP), photochemical oxidant formation potential: ecosystems (EOFP), and water consumption potential (WCP). For direct comparison, the obtained results were normalized with the highest values among the modeled systems as 100%. **d** The mortality rate and **e** developmental morphology of zebrafish embryos during the 96 h of incubation. **f** Electrocatalytic removal of ACE from different kinds of water. **g** The removal efficiencies for simultaneous treatment of ACE, bisphenol A (BPA), phenol (PhOH), and 4-hydroxyphenylacetaldehyde (HAP) in the continuous-flow reactor, and TOC removal during the treatment (200 mL reactor, 25 $cm^2$ effective electrode area, 10 min hydroxyl retention time, and 20 mL $min^{-1}$ flow rate). The insert is the scheme of the continuous-flow electrocatalytic reactor. **h** Inhibition rate of *Vibrio fischeri* during the continuous-flow operation. Unless otherwise indicated, the experimental conditions are: 1.0 V vs. Ag/AgCl applied voltages, $[\text{phenolic pollutants}]_0 = 1\,\mu M$, $[pH]_0 = 7.0 \pm 0.1$, using I-BiOI@CC anode, $T = 298.15$ K. Pollutant removal and toxicity analysis experiments were conducted in triplicate, and the obtained data with standard deviation less than 5%. Data are presented as mean values +/- SD for (**d**, **f**–**h**).

strong regenerability for sustained electrocatalytic performance. While this study validates the mechanistic and electrochemical feasibility at a laboratory scale, transforming the technology into real-world wastewater treatment requires further scale-up investigations. Thus, future work is suggested: (i) up-scaling modular electrode stacks to sustain lab-scale performance for wastewater treatment with 1–10 $m^3$/h flow rates; (ii) optimizing reactor hydrodynamics to facilitate mass transfer and guarantee consistent hydraulic retention times; (iii) validating long-term stability (3–6 months) using real wastewater with fluctuating water compositions and pollutant contains; and (iii) developing cost-effective polymer recovery and purification approach to promote downstream utilization. Such scale-up investigations are crucial to assess the techno-economic feasibility and sustainability of the technology for industrial applications.

## Discussion

This study discovers an oxidant-free electrocatalytic system that enables efficient conversion of phenolic pollutants into polymerized products via iodine-mediated PCET over the I-BiOI@CC anode. Coupled experimental and computational analyses unveil the crucial roles of enriched iodine sites in electrocatalytic polymerization, which facilitate oriented adsorption of pollutants, enhance interfacial charge transfer, and serve as reversible redox mediators, enabling highly selective polymerization without chemical oxidants. DFT calculations elucidate that polymerization mainly proceeds through the thermodynamically and kinetically favored *ortho* C–O coupling route. Structure-reactivity analysis demonstrates that the polymerization kinetics primarily correlated with the electron-donating capacity and O–H bond strength of the phenolic pollutants, underscoring the dominant role of electron- and proton-transfer energies in the PCET mechanism. Owing to the mild operational potential, elimination of oxidant demand, and polymer recovery, the electrocatalytic system exhibits exceptional energy and cost effectiveness with negative carbon emissions, while demonstrating negligible biotoxicity and excellent practicality. Overall, this work offers mechanistic insights and design blueprints for developing next-generation, oxidant-free electrocatalytic systems. By integrating wastewater decontamination with pollutant valorization, this approach transforms water treatment into a sustainable process with high energy efficiency, target selectivity, and resource-recoverable purification, aligning with carbon-neutral water management goals.

## Methods

### Chemical reagents and materials

Analytical-grade chemical reagents with purities higher than 98% were purchased for this research and used as received without purification. CC was purchased as the substrate for anode preparation, which was ultrasonically cleaned to remove any impurities before use. Details are provided in Text S1.

### Material synthesis and characterization

The BiOI@CC anode was prepared on a CC substrate using an electrodeposition method. An electrochemical workstation was employed to conduct the electrodeposition with cleaned CC as the working electrode in a three-electrode system. Specifically, a mixture containing specific concentrations of $Bi(NO_3)_3$ and KI aqueous solutions (adjusted to pH 1.7 using $HNO_3$) and p-benzoquinone ethanol solution was prepared as the electrolyte. Then, the BiOI was synthesized on the CC substrate after electrodepositing at a constant applied potential of −0.1 V *vs.* Ag/AgCl for a particular duration. Notably, the synthesis of BiOI@CC was carried out using an electrolyte with a KI to $Bi(NO_3)_3$ ratio of 4:1, and a series of I-rich BiOI@CC materials were synthesized with the KI to $Bi(NO_3)_3$ ratios higher than 4:1 (e.g., 6:1, 8:1, 10:1, etc.). The I-rich BiOI@CC with KI to $Bi(NO_3)_3$ ratios of 6:1 (namely I-BiOI@CC) attained the best performance, and was chosen as the preferred one for the electrocatalytic system. For material optimization, the I-rich BiOI@CC anodes were also synthesized at different applied potentials (−0.05, −0.1, and −0.2 V vs. Ag/AgCl) and with various deposition times (2, 5, and 10 min). The I-rich BiOI@CC anode prepared in optimized conditions (KI to $Bi(NO_3)_3$ ratios of 6:1, −0.1 vs. Ag/AgCl, and 5 min deposition time), is namely I-BiOI@CC.

The synthesized I-rich BiOI@CC anodes were comprehensively characterized to reveal their properties. The morphology of the anodes was observed using transmission electron microscopy (TEM) and scanning electron microscopy (SEM). The chemical composition and elemental state of the anodes were revealed by X-ray photoelectron spectroscopy (XPS). The surface functional groups, lattice expansion, and crystal structure of the anodes were investigated using Fourier transform infrared (FTIR) spectroscopy, Raman spectroscopy, and X-ray diffraction (XRD), respectively. Moreover, an electrochemical workstation was employed to study the electrochemical properties of the anodes by various approaches: the charge transfer ability was evaluated using EIS; electrochemical surface area (ECSA) and oxidation peaks were analyzed using cyclic voltammograms (CV); and the reactivity of the anodes at various applied potentials was measured using linear scanning voltammetry (LSV). Detailed information for electrocatalytic characterization is provided in Text S2.

### Electrocatalytic oxidation experiments

The electrocatalytic removal of phenolic pollutants was evaluated in batch experiments. The system consisted of a conventional three-electrode electrochemical cell with the as-prepared anodes as the working electrode, a Pt plate as the counter electrode, and an Ag/AgCl electrode as the reference electrode. The performance of synthesized anodes was compared using ACE as the target pollutant to identify the optimal anode. The effect of applied potential (0–1.0 V vs. Ag/AgCl) and initial ACE concentration on removal efficiency was then investigated to determine the preferred operational parameter. To highlight the advantage of the modification, the performances of CC, BiOI@CC, and the I-BiOI@CC anode were systematically compared. The broad feasibility of the system for treating phenolic pollutants was further tested with ten phenolic pollutants: ACE, phenol (PhOH), 2,6-dimethylphenol (DMP), 4-hydroxybenzoic acid (HBAc), 4-chlorophenol (4-CP), 4-nitrophenol (4-NP), bisphenol A (BPA), 4-hydroxyphenylacetaldehyde (HAP), 4-methoxyphenol (MeP) and methylparaben (MHB). The effects of water matrix on the performance of electrocatalytic polymerization and the continuous-flow operation were also studied, with details in Text S3.

### Analytical methods

The concentration of phenolic pollutants was monitored periodically by high-performance liquid chromatography (HPLC) with detailed operational parameters in Table S13. The removal kinetics were analyzed using a pseudo-first-order model: $\ln(C_t/C_0) = -k_{obs}t$, where $C_0$ and $C_t$ are the concentrations at initial time and time t, respectively, and $k_{obs}$ is the rate constant ($min^{-1}$). To reveal the mechanistic insights of electrocatalytic polymerization through PCET, multiple experiments were conducted. Electron paramagnetic resonance (EPR) with DMPO as a spin trap was employed to confirm the formation of phenoxy radicals. The radical generation was quantified using TEMPO as a chemical probe, with Liquid chromatography-mass spectrometry (LC/MS) for product identification. Scavenger tests were conducted using FA (for phenoxyl radicals), $AgNO_3$ (for iodine sites), and methanol (for $^{\bullet}OH$). The PCET pathway was verified by Nernstian shift analysis, monitoring the anodic peak potential ($E_{pa}$) of the pollutants against pH, and by kinetic isotope effect experiments comparing degradation rates of phenol and deuterated phenols ($C_6H_5OH$, $C_6D_6OH$, and $C_6D_6OD$). Cyclic voltammetry (CV) was performed to examine electrochemical behavior during polymerization. Moreover, the Marcus-Hush theory was employed to study the PCET kinetics and thermodynamics of the I-BiOI@CC anode towards different phenolic pollutants, with detailed information listed in Text S4. The Random Forest machine learning method was employed to analyze the contributions of different properties of phenolic pollutants on the thermodynamics of electrocatalytic polymerization. Detailed information on machine learning is provided in Text S5.

The polymerization products were analyzed at the molecular level. LC-MS and Matrix-assisted laser desorption/ionization time-of-flight mass spectrometry (MALDI-TOF/MS) were used to identify the formed polymer, while XPS was employed to characterize the chemical bonds (e.g., C–O–C, C–C) in the solid polymers. The dynamics of the polymerization process were observed in real time using in-situ FTIR. The stability of the anode material was assessed by measuring the leaching of $Bi^{3+}$ and $I^-$ ions during continuous-flow operation using ICP-MS.

### DFT calculations

DFT calculations were performed to model the adsorption of phenolic pollutants on the anode surfaces, calculate the corresponding adsorption energies and I–H bond lengths, and visualize the electron density difference. The Gibbs free energy of the polymerization process was also computed to explicate the role of I-rich modification. Details of DFT calculations are provided in Text S6. For the polymerization mechanism, the Gibbs free energy change during the C–O and C–C coupling processes were determined by the Gaussian 16 W software. The Gaussian 16 W software was also deployed to calculate the highest occupied molecular orbital, lowest unoccupied molecular orbital, and energy changes of proton and electron loss. Text S7 shows the information for Gaussian calculations.

### Sustainability and toxicity assessment

The economic and environmental implications of electrocatalytic polymerization were evaluated through sustainability assessment in terms of energy consumption (Text S8), cost (Text S8), and LCA analysis (Text S9). The biotoxicities of the phenolic pollutants before and after treatment by the electrocatalytic system using different anodes were assessed using the zebrafish embryo development tests, and the toxicity of the treated effluent by continuous-flow operation was assessed using *Vibrio fischeri* inhibition experiments, with details in Text S10. The zebrafish embryo development tests were conducted on zebrafish embryos and larvae stages within 96 h post-fertilization, before the independent feeding stage (120 h post-fertilization). According to the EU Directive 2010/63/EU on the protection of animals used for scientific purposes, zebrafish are not considered protected animals until they reach the stage of independent feeding. Therefore, no special license for formal animal ethics approval was required for this study.

### Reporting summary

Further information on research design is available in the Nature Portfolio Reporting Summary linked to this article.

## Data availability

The data that support the findings of this study are presented in the main text and the supplementary information. Source data are provided with this paper[44]. Link: https://doi.org/10.6084/m9.figshare.31024012 Source data are provided with this paper.

## References


1. Cheng, M. et al. Hydroxyl radicals based advanced oxidation processes (AOPs) for remediation of soils contaminated with organic compounds: a review. *Chem. Eng. J.* **284**, 582–598 (2016).
2. Kanakaraju, D., Glass, B. D. & Goh, P. S. Advanced oxidation process-mediated removal of pharmaceuticals from water: a review of recent advances. *Environ. Sci. Pollut. Res.* **32**, 14316–14350 (2025).
3. Zheng, Z. et al. Facilitating peroxymonosulfate activation for effective antibiotics degradation from drinking water by photo-electrocatalytic system using $MoS_2$ embedded carbon substrate. *Chem. Eng. J.* **452**, 139591 (2023).
4. Zheng, Z. et al. Directional separation of highly reductive electrons to the reactive center in a magnetic S-Scheme $ZnFe_2O_4$/A-$MoS_2$ heterojunction for enhanced peroxymonosulfate activation toward pharmaceuticals and personal care product removal. *Environ. Sci. Technol.* **57**, 8414–8425 (2023).
5. Qian, J., Zhang, X., Jia, Y., Xu, H. & Pan, B. Oxidative polymerization in water treatment: chemical fundamentals and future perspectives. *Environ. Sci. Technol.* **59**, 1060–1079 (2025).
6. Zhao, X. & Zhang, Z. Heterogeneous peroxymonosulfate-based advanced oxidation mechanisms: new wine in old bottles? *Environ. Sci. Technol.* **59**, 5913–5924 (2025).
7. Zhang, Y.-J. & Yu, H.-Q. Mineralization or polymerization: that is the question. *Environ. Sci. Technol.* **58**, 11205–11208 (2024).
8. Liu, C., Wu, B. & Chen, X. Sulfate radical-based oxidation for sludge treatment: a review. *Chem. Eng. J.* **335**, 865–875 (2018).
9. Chen, Y. et al. Transformative removal of aqueous micropollutants into polymeric products by advanced oxidation processes. *Environ. Sci. Technol.* **58**, 4844–4851 (2024).
10. Zhang, Y.-J. et al. Metal oxyhalide-based heterogeneous catalytic water purification with ultralow $H_2O_2$ consumption. *Nat. Water* **2**, 770–781 (2024).
11. Rui, J. et al. Revolutionizing water treatment: polymerization pathways in advanced oxidation processes. *Appl. Catal. B: Environ.* **380**, 125747 (2025).
12. Liu, Y.-Q. et al. Magnesium oxide-supported single atoms with fine-modulated steric location for polymerization transfer removal of water pollutants. *Environ. Sci. Technol.* **59**, 880–891 (2025).
13. Liu, H.-Z. et al. Tailoring d-band center of high-valent metal-oxo species for pollutant removal via complete polymerization. *Nat Commun* **15**, 2327 (2024).
14. Zuo, S. et al. Rethinking strategies to attenuate organic pollutants: Mechanisms and challenges of catalytic pollutants polymerization. *Crit. Rev. Env. Sci. Tec.* **55**, 169–189 (2025).
15. Du, X. et al. Nanostructured electrodes for electrocatalytic advanced oxidation processes: from materials preparation to mechanisms understanding and wastewater treatment applications. *Appl. Catal. B: Environ.* **296**, 120332 (2021).
16. Hu, W. et al. Electrocatalytic oxidation for organic wastewater: Recent progress in anode material, reactor, and process combination. *Chem. Eng. J.* **496**, 154120 (2024).
17. Sjödin, M. et al. Kinetic effects of hydrogen bonds on proton-coupled electron transfer from phenols. *J. Am. Chem. Soc.* **128**, 13076–13083 (2006).
18. Tyburski, R., Liu, T., Glover, S. D. & Hammarström, L. Proton-coupled electron transfer guidelines, fair and square. *J. Am. Chem. Soc.* **143**, 560–576 (2021).
19. Li, J.-Y. et al. Abatement of aromatic contaminants from wastewater by a heat/persulfate process based on a polymerization mechanism. *Environ. Sci. Technol.* **57**, 18575–18585 (2023).
20. Sajjad, M., Singh, N. & Larsson, A. Bulk and monolayer bismuth oxyiodide (BiOI): excellent high temperature p-type thermoelectric materials. *AIP Adv.* **10**, 075309 (2020).
21. Wu, Z. et al. Internal electric field enhancement by the I-Rich surface of highly crystallized bioi nanosheets for boosted photocatalytic degradation of phenol. *Small Struct.* **4**, 2200380 (2023).
22. Zhang, P.-F. et al. Relocating conjugated 2P valence electrons in carbon host to stabilize $I^+$ for Novel Zn-$I_2$ battery. *Adv. Energy Mater.* **15**, 2404845 (2025).
23. Li, L. et al. Densely packed and vertically oriented covalent organic framework membrane enabled efficient ion sieving for zinc iodine battery. *Nano Energy* **138**, 110886 (2025).
24. Soni, V. et al. Unveiling cutting-edge developments in defective BiOI nanomaterials: Precise manipulation and improved functionalities towards bolstered photocatalysis. *Adv. Coll. Interface Sci.* **340**, 103467 (2025).
25. Wu, Z. et al. Epitaxial $BiP_5O_{14}$ layer on BiOI nanosheets enhancing the photocatalytic degradation of phenol via interfacial internal-electric-field. *Appl. Catal. B: Environ.* **307**, 121153 (2022).
26. Zhang, J. et al. Selective generation of Co (IV)=O in-situ on cobalt-doping $MoS_2$@CC photoanode through photoelectrochemical activation of peroxymonosulfate for efficient antibiotic degradation. *Chem. Eng. J.* **503**, 158606 (2025).
27. Sial, A. et al. Multifaceted synergism of dual active sites in oxygen vacancies enriched plasmonic Ag-BiOI nanosheets for enhanced piezo-photocatalytic degradation of trimethoprim. *ACS ES&T Eng.* **4**, 2923–2937 (2024).

28. Zuo, S., Wang, Y., Wan, J., Ma, Y. & Yan, Z. Facilitating proton coupled electron transfer reaction through the interfacial micro electric field with Fe-$N_4$-C in FeMOFs glass. *Small* **20**, 2307102 (2024).
29. Duan, P.-J. et al. Polymeric products deactivate carbon-based catalysts in catalytic oxidation reactions. *Nat. Water* **3**, 178–190 (2025).
30. Zhdankin, V. V. & Stang, P. J. Chemistry of polyvalent iodine. *Chem. Rev.* **108**, 5299–5358 (2008).
31. Wang, X., Zheng, Z., Man, J. H. K. & Lo, I. M. C. Regulating charge transfer for enhanced PAA activation over sulfur-doped magnetic $CoFe_2O_4$: a novel strategy for simultaneous micropollutants degradation and bacteria inactivation. *Water Res.* **256**, 121595 (2024).
32. Zheng, W. et al. Trace $Br^-$ inhibits halogenated byproduct formation in saline wastewater electrochemical treatment. *Environ. Sci. Technol.* **58**, 12212–12224 (2024).
33. Chen, L. et al. Accurate identification of radicals by in-situ electron paramagnetic resonance in ultraviolet-based homogenous advanced oxidation processes. *Water Res.* **221**, 118747 (2022).
34. Li, M. et al. Surface FeIV=O induced highly selective phenol polymerization via proton-coupled electron transfer. *J. Am. Chem. Soc.* **147**, 31165–31174 (2025).
35. Xie, C., Liu, Y., Lu, W., Zhang, H. & Li, X. Highly stable zinc–iodine single flow batteries with super high energy density for stationary energy storage. *Energ. Environ. Sci.* **12**, 1834–1839 (2019).
36. Bai, C.-W. et al. Circumventing bottlenecks in $H_2O_2$ photosynthesis over carbon nitride with iodine redox chemistry and electric field effects. *Nat. Commun.* **15**, 4718 (2024).
37. Wu, J.-H. et al. Tailoring the selective generation of oxidative organic radicals for toxic-by-product-free water decontamination. *Proc. Natl. Acad. Sci. USA.* **121**, e2403544121 (2024).
38. Jiang, S., Zhang, Y. & Gong, J. Applications of bismuth-based nanoparticles for the removal of pollutants in wastewater: a review. *Environ. Sci. Nano* **11**, 1332–1367 (2024).
39. Zhang, Y.-J. et al. Simultaneous nanocatalytic surface activation of pollutants and oxidants for highly efficient water decontamination. *Nat Commun.* **13**, 3005 (2022).
40. Lu, T. & Chen, F. Bond order analysis based on the laplacian of electron density in fuzzy overlap space. *J. Phys. Chem. A* **117**, 3100–3108 (2013).
41. Yu, J., Su, N. Q. & Yang, W. Describing chemical reactivity with frontier molecular orbitalets. *JACS Au.* **2**, 1383–1394 (2022).
42. Zhi, W., Appling, A. P., Golden, H. E., Podgorski, J. & Li, L. Deep learning for water quality. *Nat Water* **2**, 228–241 (2024).
43. Zheng, Z., Man, J. H. K. & Lo, I. M. C. Integrating reactive chlorine species generation with $H_2$ evolution in a multifunctional photoelectrochemical system for low operational carbon emissions saline sewage treatment. *Environ. Sci. Technol.* **56**, 16156–16166 (2022).
44. Zheng, Z. et al. Iodine mediated proton–coupled electron transfer enables selective polymerization of organic pollutants in an oxidant free electrocatalytic system. Data sets, *Figshare*,https://doi.org/10.6084/m9.figshare.31024012 (2026).


## Acknowledgements

The authors appreciate the financial support from the Research Grants Council (RGC, Hong Kong) through the General Research Fund (16204823).

## Author contributions

Zexiao Zheng: conceptualization, methodology, investigation, data analysis, validation, writing—original draft. Jin Zhang: methodology, investigation, data analysis, validation, writing—review & editing. Jonathan J. Calvillo Solís: investigation, validation, writing—review & editing. Howard Y.M. Cheung: validation, writing—review & editing. Ashutosh Kumar: writing—review & editing. Xiaohong Guan: writing—review & editing. Haoran Dong: writing—review & editing. Irene M.C. Lo: funding acquisition, project administration, methodology, supervision, validation, writing—review & editing.

## Funding

Zexiao Zheng, Jin Zhang, Jonathan J. Calvillo Solís, Howard Y.M. Cheung, and Irene M.C. Lo disclose support for the research of this work from the Research Grants Council (RGC, Hong Kong) [grant number GRF 16204823. Ashutosh Kumar, Xiaohong Guan, and Haoran Dong declare no relevant funding.

## Competing interests

The authors declare no competing interests.

## Additional information

**Supplementary information** The online version contains supplementary material available at https://doi.org/10.1038/s41467-026-74349-6.

**Correspondence** and requests for materials should be addressed to Jin Zhang or Irene M. C. Lo.

**Peer review information** *Nature Communications* thanks the anonymous reviewers for their contribution to the peer review of this work. A peer review file is available.